Magnetic Stars, 2011, pp. 229 – 238

Magnetic Field of Young Star RW Aur

Dodin A. V.[1], **Chountonov G. A.**[2], **Lamzin S. A.**[1]

[1] Sternberg Astronomical Institute, Moscow, Russia
[2] Special Astrophysical Observatory, Nizhny Arkhyz, Russia

Abstract. We report new results of spectropolarimetric magnetic field measurements for the classical T Tauri star RW Aur. We have found the longitudinal magnetic field $|B| \sim 1\,\mathrm{kG}$ in RW Aur A. The field strength in an accretion spot (He I line) varies from -1.5 to $+1.1\,\mathrm{kG}$. The observations and the evolutionary stage of RW Aur hint at a complicated field topology for the star. A magnetic field up to 1 kG was found in the warm part of the RW Aur A outflow traced by Na I D lines. The field has not been found in the hot part of the outflow, where the broad emission component of He I 5876 Å line is formed.

Key words: CTTS – magnetic field – accretion – RW Aur

1 Introduction

CTTSs are young ($t < 10^7$ yr) low–mass ($M \leq 2M_\odot$) pre–main sequence stars, accreting matter from a protoplanetary accretion disk. A crucial difference between the current model of accretion onto the young stars, and previous models is the magnetic field, which governs the motion of accreting matter within a truncation radius (i.e. approximately an alfvenic radius). Therefore, the field topology and strength are important in order to understand the accretion and ejection processes and the evolution of stellar angular momentum. Moreover, field measurements are necessary to test the field generation theories. In the earliest models of magnetospheric accretion (Camenzind, 1990; Romanova et al., 2003), the field was supposed to be dipolar; however, recently a complex magnetic field has been discovered by means of the Zeeman Doppler Imaging (Donati et al., 2008).

RW Aur is one of the brightest CTTS. A description of photometric and spectral properties of the star can be found in Petrov's paper (Petrov et al., 2001). To cut a long story short, this star is highly variable due to several sources of variability and possesses a multi–component spectrum: photospheric lines, broad emission lines, narrow emission lines, P Cygni and inverse P Cygni lines, continuum excesses. Some features can be explained in the model of magnetospheric accretion, but many features are contradictory or unexpected for the current model. For example, wild photometric behavior, or the width of "narrow" emission lines and many other puzzles.

The first field detection for RW Aur has been reported in Symington et al. (2005), but it was based on only one observation and at 2σ level: $0.46 \pm 0.21\,\mathrm{kG}$. In our paper, we report new results of spectropolarimetric magnetic field measurements for RW Aur. The method is based on the fact that in the case of Zeeman splitting of the so–called σ component, the lines are polarized circularly, with oppositely polarized components being located on different sides of the central wavelength λ_0. If the magnetic field in the line formation region has a longitudinal component $B_{||}$, then the lines observed in the right– and left–hand polarized light will be shifted relative to one another by

$$\Delta\lambda = 9.3 \cdot 10^{-10} g \lambda_0^2 B_{||} \qquad \text{mÅ}, \tag{1}$$

Table 1: The observational log

JD 245...	Band, Å	SNR
3746.30	5575.7 – 5941.6	367
3748.30	5575.2 – 5941.2	791
3749.33	5575.1 – 5941.2	515
3784.29	5741.2 – 6107.2	453
3784.41	6166.6 – 6532.1	367
3786.43	5743.7 – 6109.5	393
3786.49	6169.0 – 6534.3	297
4460.26	5585.2 – 5951.1	425
4460.69	5599.0 – 5964.9	377
4460.56	6074.2 – 6439.7	585
4461.25	5599.1 – 5965.1	563
4461.41	6075.4 – 6440.9	669
4461.56	5630.6 – 5996.5	607
4461.68	6070.9 – 6436.4	321
4486.27	5737.4 – 6103.2	466
4486.47	6218.3 – 6583.5	593
4846.34	5796.0 – 6161.8	476
4846.44	6247.2 – 6612.3	505

JD — Julian date

SNR — the signal–to–noise ratio

where g is the Lande factor of the line under consideration. The wavelength in Eq. 1 is in Å and $B_{||}$ is in G. This relation allows the longitudinal magnetic field component averaged over the line formation region to be found by measuring $\Delta\lambda$ from two spectra taken in the right– and left–hand polarized light.

2 Observations and Data Analysis

The spectra were obtained at the 6–m BTA telescope of the Special Astrophysical Observatory with the Main Stellar Spectrograph (Panchuk, 2001) equipped with a circular polarization analyzer (Chountonov, 1997) during several observational sets (see Table 1). The spectrograph slit width, $0\farcs5$, provided spectral resolution of $R \sim 15000$. Exposure time was about 20 minutes.

The spectra were processed as follows. Dark current, night sky emission and detector bias, as well as cosmic ray traces were removed in a standard way, using the routines from the MIDAS software package (Smirnov et al., 2003). A spectrum of a thorium–argon lamp was used for the wavelength calibration. The spectra are transformed into the stellar rest frame, i. e. the Earth radial velocity and the average radial velocity of RW Aur (+16 km/s) are subtracted (Petrov et al., 2001).

RW Aur is a binary star, but the secondary component is negligible in the visual band and spectral lines (Petrov et al., 2001).

To measure the difference between the line positions in the spectra with opposite polarizations, we used a version of the cross-correlation method described in detail, for example, by Johnstone and Penston (1986), for the confidence level $\alpha = 0.68$ corresponding to 1σ error. The shifts were measured in pixels and converted to Å using the calibration of the spectrum.

To take into account the systematic instrumental errors, the observations were organized as

follows. Between the exposures, the phase compensator rotated in such a way that the right– and left–hand polarized spectra on the CCD array interchanged. Let $\Delta\lambda_{rl}^{(1)}$ be the difference between the positions of a certain line in the spectra with opposite polarizations measured at the initial position of the phase compensator, and $\Delta\lambda_{rl}^{(1)}$ be the same quantity measured after the compensator's rotation. Then, the quantity

$$\Delta\lambda_{rl} = \frac{\Delta\lambda_{rl}^{(2)} - \Delta\lambda_{rl}^{(1)}}{2} \tag{2}$$

will be free from systematic errors, with the main error being the spectrograph slit tilt. Thus, two exposures of the star are required to measure the line shift.

We observed two targets to test our instrumental set–up and the data reduction process — the magnetic star 53 Cam and a giant "zero" field star (HD 33256). In case of 53 Cam, the field strength we derived was $B = 0.34 \pm 0.11$ kG, that is consistent with the predicted $B = 0.36$ kG (Hill et al., 1998). In one field measurement of HD 33256 $B = -0.18 \pm 0.06$ kG has been found, the result consistent with the expected zero field at the 3σ level, but we suppose a possibility of a false field detection with a longitudinal component $|B| < 0.2$ kG. To control the systematic errors of target lines we measure the field in the forbidden line [O I] 6300 Å with the expected zero field and photospheric lines. The corresponding values are presented in Table 4.

3 RW Aur Spectra

The observed spectrum of the star includes features related with the ongoing accretion and the photospheric spectrum. The accretion features are blended with photospheric lines, which complicates the analysis of the accretion. To carefully explore the non-photospheric lines, the photospheric spectrum must be eliminated. To take into account the photospheric features, generally speaking, a detailed model of the stellar atmosphere with a hot spot, as well as a model of surrounded gas is needed. It means that in order to separate the photospheric and non-photospheric emission, a combined SED of all the sources must be simulated. Simplifying the problem, we do not consider an interplay between the photospheric and non–photospheric emission, i. e. the SED is an algebraic sum of both SEDs. This approximation is good enough for an optical thin non–photospheric emission, or in case of non–overlapping formation regions of both components. In our case, the method allows us to remove a significant part of photospheric absorptions, which distort the profiles important for our analysis, and to determine the uncertainties of parameters resulting from the photospheric lines.

The photospheric spectrum is unknown, but there exist estimations of spectral class for RW Aur between K1 and K4 (Petrov et al., 2001). We used a spectrum of the K1IV star HD 138716, adopted from the UVES library (Bagnulo et al., 2003). This spectrum was transformed into the stellar rest frame via its comparison with the theoretical one from the VALD database (Kupka et al., 1999). The spectrum was broadened to the line width of RW Aur's spectrum by convolution with the Gaussian with $\sigma = 20$ km/s. A veiling was found approximately by a comparison of weak absorption lines of RW Aur with the lines of HD 138716.

After removing the photospheric lines we can analyze the spectrum of the accreting gas.

3.1 He I 5876 Å Line Profile

The most promising tool for our analysis is the He I 5876 Å line. The line has a fine structure: 6 components with the maximal difference of about 20 km/s. The wavelength 5875.6 Å is accepted to be the central wavelength. The line profile of He I 5876 Å has 3 components:

1. A broad red–shifted absorption component. This component in the magnetospheric accretion model is formed in the hot region of pre–shock gas, where the velocity is about 400 km/s. In case

Table 2: He I 5876 Å. Parameters of the red–shifted absorption.

JD 245...	r_v	EW	ΔEW	V_c	ΔV_c
3746.30	0.6	0.070	0.032	326.6	21.8
3748.30	1.6	0.722	0.050	228.1	0.7
3749.33	1.6	0.306	0.043	256.0	0.4
3784.29	3.6	0.060	0.024	316.7	13.8
3786.43	2.0	0.216	0.046	198.8	9.7
4460.26	0.9	0.252	0.042	265.8	0.2
4460.69	2.0	0.134	0.038	291.6	5.5
4461.25	2.0	0.260	0.037	272.0	0.4
4461.56	2.5	0.634	0.043	229.1	0.7
4486.27	1.0	0.026	0.012	362.5	10.5
4846.34	1.4	0.164	0.042	271.8	1.2

JD — the Julian date, r_v — the mean veiling, EW, V_c, ΔEW, ΔV_c — the equivalent width and the center velocity of the red–shifted absorption and the corresponding uncertainties.

of a well–collimated accretion stream, we should observe one narrow line with the central velocity between 0 and 400 km/s, depending on the stream orientation relative to the line of sight. However, the observations show one broad line, which occupies the whole region of 0 – 400 km/s. It indicates a strong divergence of the accretion flow: we simultaneously observe fluid tubes, which penetrate into the photosphere at different angles. The central velocity of this line shows a small variability (see Table 2), which is probably related with the non–axisymmetric accretion zone relatively to the stellar rotation axis. The magnetic field in this region is equal to the field in the accretion zone on the stellar surface. However, due to the projection effect, the longitudinal component linearly changes over the profile: $B_{||} \sim V_{||}$. The field in this component is difficult to measure due to the small slope of the profile.

2. A narrow emission component at zero velocity. This component is formed in a post–shock region near the stellar photosphere. FWHM of the component is variable, equal to about 70 km/s. The component is thought to be formed in the strong field region, however, due to the strong divergence of field lines (see above), the measured longitudinal field should be smaller than the absolute field due to the projection effect. This effect could be taken in to account since the angular distribution of the field could be deduced from the red–shifted absorption. However, we do not have a good model to describe the red–shifted absorption and to solve the inverse problem related to it.

3. A broad emission component. FWHM of the component is about 200 km/s. The velocity of the line center lies between −90 and 10 km/s. It is reasonable to relate this component with a non-axisymmetric outflow. Therefore, the field in the broad component is significantly smaller than the one in the narrow component.

A veiling around the He I 5876 Å line is defined as a simple mean over two bands, 5840 – 5870 Å and 5910 – 5920 Å. For each band a veiling was determined by the least–squares method using the spectrum of HD 138716 as a template. The obtained veiling, an equivalent width EW, and the central velocity V_c of the broad absorption are presented in Table 2. All the values were calculated after the removal of photospheric lines. The uncertainties of the values are determined by the veiling uncertainty, which can reach factor 2. We calculated EW and V_c for the upper and lower limits of the veiling. The half–sum and half–residual of the EW or V_c for both veiling determine the mean EW or V_c and corresponding uncertainties for these values.

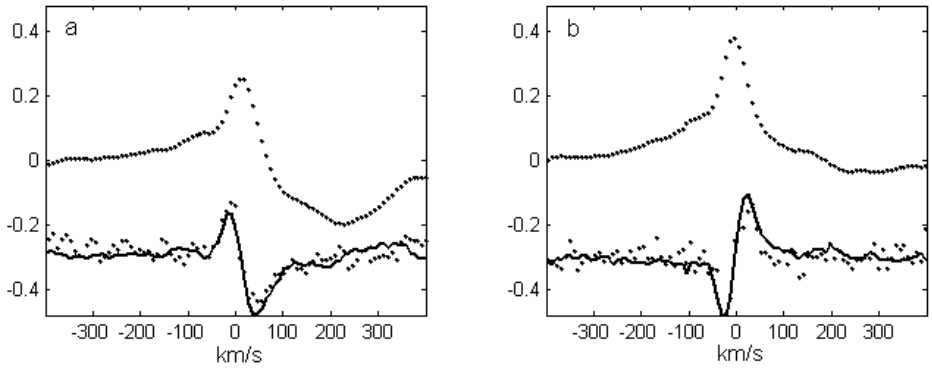

Figure 1: I/I_c and V profiles of He I 5876 Å line in case of the extreme negative (a) and extreme positive (b) field strength, the dots represent the observational profiles, the solid line reproduces a semi–empirical V profile, the V profiles were multiplied 10 times and shifted to -0.3.

3.2 Na I D Lines

Each line in the doublet includes a few components:
1. A broad absorption component resembling the absorption component in He I 5876 line.
2. A blue–shifted broad emission component.
3. A blue–shifted absorption component. This absorption is blended with the emission (2) and they form a P Cygni profile.
4. A photospheric absorption and an interstellar absorption. Both lines contribute significantly to the absorption component in the P Cygni profile, but they do not dominate.

Thus, the Na I D lines are formed in the stellar wind as well as in the accretion flow. One unexpected result was the field detection in the component, related with the outflow.

3.3 [O I] 6300Å Line

Three kinematic components of the forbidden oxygen line are observed. The line emission is formed in the low-density gas at large distances from the star, where the field strength is close to zero. This line is suitable to control the errors of our method. However, there is one fact that complicates the matter: the oxygen line is slightly blended with the photospheric lines.

3.4 Emission Lines of Metals

Numerous emission lines of metals are observed in the spectrum. The lines do not reveal any accretion signatures (i. e. inverse P Cygni) or ejection signatures (i. e. P Cygni). FWHM is about 100 km/s. The broad emission component is often blended with the photospheric one.

4 Field Detections

4.1 He I 5876 Å Emission Components

The averaged over emission part of the He I 5876 Å line profile strength of the longitudinal magnetic field was determined using the cross–correlation method. The value of the Lande factor adopted for He I line 5876 Å was 1.11 (Johns–Krull et al., 1999).

The results are presented in Table 3. A part of the line profile, based on which the field was determined, contains only the emission components of the line. The red–shifted absorption was

Table 3: The field measured from He I 5876 Å.

	He I 5876 Å				Na I 5893 Å		Fe I 5659 Å		The photosphere	
JD 245...	B	ΔB	σ	$B(\delta\lambda)$	B	ΔB	B	ΔB	B	ΔB
3746.30	−0.43	0.25	0.09	−0.57	0.11	0.11	0.17	0.30	0.24	0.10
3748.30	−1.47	0.15	0.03	−1.51	−0.24	0.06	−0.15	0.30	0.07	0.20
3749.33	−1.01	0.20	0.07	−1.10	−1.08	0.11	−0.10	0.36	0.18	0.30
3784.29	1.10	0.15	0.01	1.21	−0.04	0.11			−1.27	0.40
3786.43	−0.11	0.35	0.32	−0.18	0.17	0.11			−0.07	0.30
4460.26	−0.82	0.25	0.05	−0.95	0.06	0.11	0.36	0.30	0.32	0.30
4460.69	−0.98	0.25	0.04	−1.30	−0.03	0.11	0.64	0.42	0.04	0.30
4461.25	−1.04	0.15	0.03	−1.28	0.03	0.11	0.47	0.36	0.12	0.20
4461.56	−1.11	0.15	0.03	−1.14	0.12	0.06	0.11	0.48	0.09	0.20
4486.27	0.50	0.20	0.06	0.82	−0.14	0.11			0.11	0.20
4846.34	−1.19	0.15	0.06	−1.27	0.04	0.11			0.08	0.10

JD — the Julian date. B, ΔB — the field and its corresponding uncertainty, in kG. σ — the mean–square residual of the observational $B(\Lambda)$ and predicted one, in case of "zero" field in the broad component, in kG. $B(\delta\lambda)$ — the field corresponds to the Zeeman shift of the narrow Gaussian, which results in the equality of the observational field, averaged over the line profile and the expected one, kG (see text for details).

excluded from the cross–correlation procedure. Figure 1 demonstrates the Stokes vectors I, V for the cases of the maximum positive and maximum negative field. The He I 5876 Å line profile in the case of a positive field differs from the profiles according to the negative field in the depth of the red–shifted absorption component. The shallow red–shifted absorption component corresponds to the positive field, and vice versa, a deep absorption — a negative field. We plotted the field strength versus the equivalent width of the red absorption on Fig. 2. The correlation coefficient of these values is -0.66 ± 0.17.

If we suppose a constant field over the line profile with the strength defined above, then a semi–empirical Stokes V can be defined as $L(\lambda) - L(\lambda + \delta\lambda)$, where L is a spectrum with left circular polarization, $\delta\lambda$ is a shift determined by the cross–correlation method. This semi–empirical V is put together with the observational V. A comparison of both profiles gives a reason to assert that the field in a broad component with the strength equal to the strength in the narrow component has an insignificant effect in the Stokes V due to the small slope of the broad component.

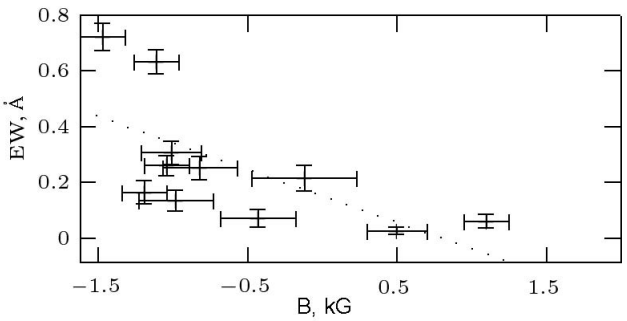

Figure 2: The correlation of the equivalent width of the red–shifted absorption and the longitudinal field component.

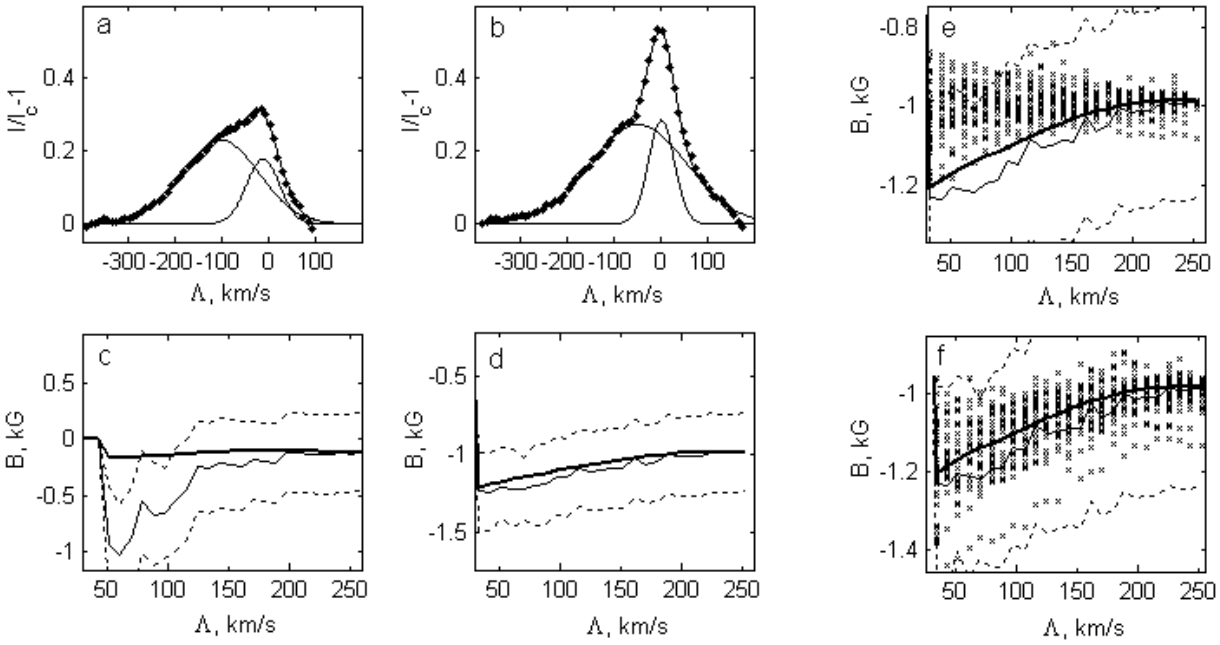

Figure 3: (a,b) — the I/I_c profiles for the He I 5876 Å line, the dots — the observational profile, the solid bold line — fitting Gaussians, (c,d) — the function $B(\Lambda)$, the solid tiny line — the observational $B(\Lambda)$, the dashed lines — 1σ bounds of the observational curve $B(\Lambda)$, the solid bold line — the predicted curve in case of the absence a field in the broad component. a, c — for the worst coincidence of the observational curve and the predicted one $B(\Lambda)$ (JD 2453786.4); b, d — a good coincidence of the curves (JD 2454460.7). (e,f) — the test 1 and 2 correspondingly (JD 2454460.7), the crosses are the predicted curves $B(\Lambda)$ for the noised model profile.

In order to determine the field strength in the broad component, we consider a dependence between the field strength B_i and a part of the profile Λ_i, based on which the field B_i was measured. In case of a constant field over the profile, the measured strength B_i is independent of the part of profile. The measurements revealed that the field strength is converged to zero when we increase a part of the broad component in the line profile.

An emission profile of He I 5876 Å can be approximated by the sum of narrow and broad Gaussians, which correspond to the narrow and broad components. Let us repeat the procedure of field measurement for the sum of Gaussians. The field is supposed to be present in the narrow Gaussian $g_1(\lambda)$, while in the broad Gaussian $g_2(\lambda)$ the field is equal to zero. That is, we cross–correlate two vectors: $L = g_1(\lambda) + g_2(\lambda)$ and $R = g_1(\lambda + \delta\lambda) + g_2(\lambda)$ over the wavelength range Λ_i. The first member of the sequence Λ_i contains 9 points of the profile, it corresponds to the velocity range of about 75 km/s, centered at the top of the narrow Gaussian. Each next member Λ_i is wider than the previous one and the last member contains the whole range of λ of the emission part of profile. At first, the range of Λ_i expands in both directions. When the red bound of Λ_i reaches the blue bound of the red–shifted absorption, Λ_i expands only in blue direction. After a series of field measurements the sequence of $B_i^T = B(\Lambda_i, \delta\lambda)$ was obtained. To define $\delta\lambda$, we normalize: the averaged theoretical field is equal to the averaged observational field, $B_{end}^T(\delta\lambda) = B_{end}$.

Approximately in a half of cases the $B(\Lambda)$ curve is well consistent with its theoretical curve $B^T(\Lambda)$. In the rest of cases, at small widths of Λ_i, a modulus of the observational values $B(\Lambda)$ is larger than the modulus of expected values $B^T(\Lambda)$, but never smaller. In Table 3 a mean–square

Table 4: The field in [O I], Si II, Fe I.

	O I 6300 Å		Si II 6347 Å		Si II 6371 Å		Fe I 6192 Å		The photosphere	
JD 245...	B	ΔB	B	ΔB	B	ΔB	B	ΔB	B	ΔB
3784.4	0.32	0.24	−0.20	0.85	−0.33	1.04	−0.75	0.40	−0.22	0.30
3786.5	−0.12	0.24	−1.60	0.57	−0.32	0.89	−0.93	0.60	0.06	0.10
4460.6	0.06	0.29	−0.22	0.38	−0.03	0.47	1.32	0.50	0.06	0.10
4461.4	−0.08	0.19	−0.45	0.33	−0.57	0.42	−0.44	1.05	0.16	0.10
4461.7	−0.09	0.19	−1.52	0.66	−0.86	0.80	0.80	1.94	0.20	0.20
4486.5	0.20	0.14	0.21	0.57	−0.15	0.28			−0.06	0.10
4846.4	0.06	0.14	−0.27	0.38	−0.95	0.42			0.03	0.10

JD — the Julian date, B, ΔB — the mean field and its uncertainty, kG.

residual of the observational $B(\Lambda)$ and the predicted one is listed. The line profiles of He I 5876 Å and the corresponding curves $B(\Lambda)$, $B^T(\Lambda)$ are presented in Fig. 3 in cases of the worst and best coincidence of the observational and predicted $B(\Lambda)$ curve.

A straight line of the mean field $B = B_{end}$ (the last member of the sequence $B(\Lambda)$) usually lies under a formal 1σ error estimated by the means developed by Johnstone and Penston (1986). Therefore, the observational shape of the curve can be induced by the noise in the spectra, which systematically imitates a strong field at narrow ranges Λ_i. To clear this problem, two statistical experiments have been carried out, each experiment containing 30 trial runs.

In the first experiment we correlate two vectors $L = g_1(\lambda) + g_2(\lambda) + n_1(\lambda)$ and $R = g_1(\lambda + \delta\lambda) + g_2(\lambda + \delta\lambda) + n_2(\lambda)$, where n_1 and n_2 — a Gaussian noise with a dispersion defined from the observational spectrum. The shift $\delta\lambda$ corresponds to the mean field. The curves $B^T(\Lambda)$ are collected around $B = B_{end}$ and have never crossed the observational $B(\Lambda)$ at small widths Λ_i (Fig. 3). Therefore, the Gaussian noise of L and R cannot induce a systematic increase of $|B(\Lambda)|$ at small widths.

In the second experiment: $L = g_1(\lambda) + g_2(\lambda) + n_1(\lambda)$ and $R = g_1(\lambda + \delta\lambda) + g_2(\lambda + 0) + n_2(\lambda)$. The curves $B^T(\Lambda)$ are collected around the theoretical and observational curve $B(\Lambda)$ (Fig. 3).

4.2 [O I] 6300 Å Line

The field was measured from three components of the oxygen line by the cross–correlation method. The Lande factor for [O I] 6300 Å is assumed to be equal to 1. This line is formed in jets and cannot show a significant field. The line is blended with the photospheric features with a depth smaller than 0.1 of the continuum level. The results of our measurements are listed in Table 4.

4.3 Na I D 5890, 5896 Å Line

The field is accurately measured in the blue part of the profile with the P Cygni absorption, while the field in the red–shifted absorption is difficult to measure due to its small slope and depth. The Lande factor is assumed to be equal to 1. The results of measurements are listed in Table 3.

4.4 Photospheric Lines

The field measurements were carried out using the line list from the VALD database (Kupka et al., 1999) for $T_{eff} = 4750$ K, $\lg g = 4$, $V_{micro} = 10$ km/s, with a depth more than 0.5. Our experience shows that such lines are still visible in a veiled spectrum of RW Aur. The lines blended by nonphotospheric

features were removed from the line list. In case of blended photospheric lines, the effective Lande factor was calculated:

$$g_{eff} = \frac{\sum d_i g_i}{\sum d_i}. \quad (3)$$

Here g_i is the Lande factor for a single line, d_i is the central depth of the line. For the lines with an undefined Lande factor in the VALD database, this factor was equated to 1. To detect a field we used our method of cross–correlation applied to the whole line list at once.

5 Discussion

Our field measurements on He I 5876 Å suggest that in seven cases the field is equal to $B \approx -1$ kG. In one case the field approaches zero $B \approx 0$ kG, which is probably induced by the broad component, dominating in that emission profile. In another case a weak negative field was registered and in two cases — a positive field, in these last three cases EW of the red absorption is less than 0.1 Å, i. e. the absorption is practically absent.

The magnetic field has changed its polarity on the time scale of less than a month; hence, two suggestions can be made:

It is reasonable to suppose that the magnetic topology has not changed significantly, but the change of sign can be explained by the accretion zones with different polarities. There is no way to reconstruct the surface magnetic map due to a deficiency in our observational data. It is reasonable to assert that the field lines, accreting the disk matter are the lines of a dipolar component, since the strength of the dipolar component changes with distance not so steeply in comparison with other multipole components. In such a picture the first accretion zone with a negative field is located near one pole, while the second zone is located near the other pole, which is invisible most of the time. When we observe a negative field, the "positive" zone is behind the star and vice versa. Using the duration t/P of the occultation phase, and the inclination of the system i we can estimate the angle between the rotational and magnetic axes φ:

$$\tan\varphi = \frac{1}{\tan i \cos \pi \dfrac{t}{P}}. \quad (4)$$

The duration t/P can be estimated statistically: for our observations the positive pole is visible in 3/11 cases. Moreover, we can use the evidence that the positive field corresponds to a shallow red–shifted absorption. Using about 60 profiles found in the literature (Alencar et al., 2005; Petrov et al., 2001; Edwards et al., 1994; Beristain et al., 2001; Muzerolle et al., 1998) and in the ELODIE archive (Moultaka et al., 2004), the duration t/P lies between 0.1 – 0.2. The inclination of RW Aur is $i = 45° - 60°$ (Cabrit et al., 2006). Therefore, $\varphi = 30° - 50°$.

However, it is possible that the field is sufficiently non–dipolar and unsteady. Such field is expected in stars with a formed radiative core (Donati et al., 2008, Donati et al, 2003). To determine the evolutionary stage of RW Aur we adopt the parameters of RW Aur from Petrov et al. (2001): $T_{eff} = 4600 - 5100$ K, $M > 1.1 M_\odot$, $L = 0.85 - 1.1 L_\odot$. Let us put the parameters on the evolutionary tracks from Siess et al. (2000). It can be seen from Fig. 4 that RW Aur has a radiative core, therefore, a complicated field topology is more probable. In case of a complex field, the matter can fall towards the star through a great number of channels. Observational evidences of the multistream accretion have been found in the ELODIE archive (Moultaka et al., 2004). Narrow absorption features are observed in the red–shifted absorption. These components are not the photospheric lines and they are not noises, because they are observed simultaneously in the He I and Na I D lines. The simplest interpretation of the observed phenomenon is the multistream accretion.

Acknowledgements. We would like to thank D. O. Kudryavtsev for assistance with our observations and D. A. Smirnov for some computer codes.

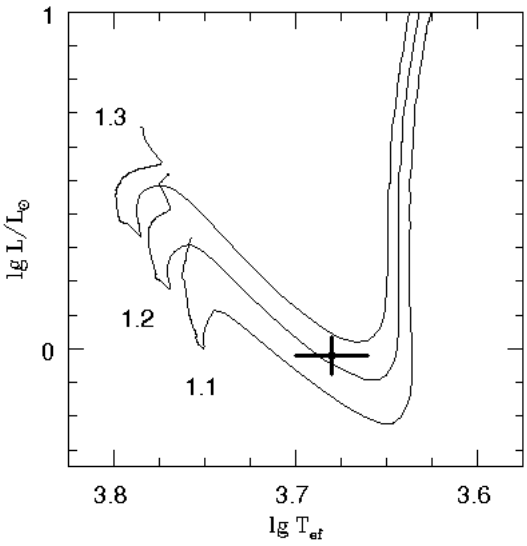

Figure 4: The position of RW Aur on the HR diagram and the evolutionary tracks from Siess et al. (2000). The numbers at the tracks are the stellar masses in $M_{\odot}$

References

Alencar S. H. P., Basri G., Hartmann L., Calvet N., 2005, A&A, 440, 595
Bagnulo S., Jehin E., Ledoux C., Cabanac R., Melo C., Gilmozzi R., The ESO Paranal Science Operations Team, 2003, The Messenger, 114, 10
Beristain G., Edwards S., Kwan J., 2001, ApJ, 551, 1037
Cabrit S., Pety J., Pesenti N., Dougados C., 2006, A&A, 452, 897
Camenzind M., 1990, Rev. Modern Astron., 3, 234
Chuntonov G. A., 1997, Annual Report of the SAO RAS, 56, 36
Donati J.–F., Cameron A. Collier, Semel M., Hussain G. A. J., Petit P., Carter B. D., Marsden S. C., Mengel M., López Ariste A., Jeffers S. V., Rees D. E., 2003, MNRAS, 345, 1145
Donati J.–F., Jardine M. M., Gregory S. G., Petit P., Paletou F., Bouvier J., Dougados C., Ménard F., Cameron A. C., Harries T. J., Hussain G. A. J., Unruh Y., Morin J., Marsden S. C., Manset N., Aurière M., Catala C., Alecian E., 2008, MNRAS, 386, 1234
Edwards S., Hartigan P., Ghandour L., Andrulis C., 1994, AJ, 108, 1056
Johnstone R. M., Penston M. V., 1986, MNRAS, 227, 797
Johns-Krull C. M., Valenti J. A., Hatzes A. P., Kanaan A., 1999, ApJ, 510, L41
Hill G. M., Bohlender D. A., Landstreet J. D., Wade G. A., Manset N., 1998, MNRAS, 297, 236
Kupka F., Piskunov N., Ryabchikova T. A., Stempels H. C., Weiss W. W., 1999, A&AS, 138, 119
Moultaka J., Ilovaisky S. A., Prugniel Ph., Soubiran C., 2004, PASP, 116, 693
Muzerolle J., Hartmann L., Calvet N., 1998, AJ, 116, 455
Panchuk V. E., 2001, Preprint of the SAO RAS, 154
Petrov P. P., Gahm G. F., Gameiro J. F., Duemmler R., Ilyin I. V., Laakkonen T., Lago M. T. V. T., Tuominen I., 2001, A&A, 369, 993
Romanova M. M., Ustyugova G. V., Koldoba A. V., Wick J. V., Lovelace R. V. E., 2003, ApJ, 595, 1009
Siess L., Dufour E., Forestini M., 2000, A&A, 358, 593
Smirnov D. A., Fabrika S. N., Lamzin S. A., Valyavin G. G., 2003, A&A, 401, 1057
Symington N. H., Harries T. J., Kurosawa R., Naylor T., 2005, MNRAS, 358, 977